Correlation of Low-Frequency Noise to the Dynamic Properties of the Sensing Surface in Electrolytes

Da Zhang,[†] Paul Solomon,[,§] Shi-Li Zhang,[†] and Zhen Zhang[*,†]*

[†]Solid-State Electronics, The Ångström Laboratory, Uppsala University, SE-751 21 Uppsala, Sweden, and [§]IBM T. J. Watson Research Center, Yorktown Heights, New York 10598, US.

KEYWORDS: low frequency noise, Solid/liquid interface, ion-sensing, site-binding model, electrochemical impedance

ABSTRACT**:** Low-frequency noise (LFN) is of significant implications in ion sensing. As a primary component of LFN for ion sensing in electrolytes, the solid/liquid interfacial noise remains poorly explored especially regarding its relation to the surface binding/de-binding dynamic properties. Here, we employ impedance spectroscopy to systematically characterize this specific noise component for its correlation to the dynamic properties of surface protonation (i.e., hydrogen binding) and deprotonation (i.e., hydrogen de-binding) processes. This correlation is facilitated by applying our recently developed interfacial impedance model to ultrathin TiO_2 layers grown by means of atomic layer deposition (ALD) on a TiN metallic electrode. With an excellent fitting of the measured noise power density spectra by the model for the studied TiO_2 layers, we are able to extract several characteristic dynamic parameters for the TiO_2 sensing surface. The observed increase of noise with TiO_2 ALD cycles can be well accounted for with an increased average binding site density. This study provides insights into how detailed surface properties may affect the noise performance of an ion sensor operating in electrolytes.

The dominant contributor to the noise in ion-/bio- sensing sensors is known to prevail in the low-frequency regime[1–4]. As such, low-frequency noise (LFN) is the primary cause responsible for limiting the resolution in sensing applications. Ion sensitive field-effect transistor (ISFET) technology finds a vast variety of applications in chemistry and biomedicine[5–7], and the LFN behavior of an ISFET has received extensive in-depth investigations[2–4,8–24]**.** On one hand, it has been shown that the LFN of the various forms of ISFETs investigated can originate from the solid-state part of the devices, in particular their conducting channel[2,8,10–12,17,20,22] or surrounding dielectric layers[19,21]. On the other hand, there is evidence showing the ISFET LFN to be a result of the adsorption/desorption events occurring at the sensing surface of the devices[3,4,16,18,23]. Our previous work[16] concludes from experimental viewpoint that the LFN originating from the solid/liquid interface is of thermal nature and its amplitude is comparable with that from the semiconductor/oxide interface.

Based on our recently developed interfacial impedance model[25] that incorporates the standard site-binding model[26], we have confirmed that the interfacial noise is directly linked to the dynamic nature of the binding/de-binding reactions of surface hydrogen ions (H^+). The present work is aimed at elucidating the correlation of the interfacial LFN to the surface dynamic properties, i.e. reaction rate constants and binding site density. This is carried out by applying our model to ultrathin TiO_2 layers grown by means of atomic layer deposition (ALD). By varying the thickness of the resulting TiO_2 layers via designing the number of deposition cycles, we are able to identify how the dynamic properties are affected by subtle changes in the structure and morphology of the sensing surface.

RRESULTS AND DISCUSSION

Noise modeling[25]

On the basis of the site-binding model[27], charging of an oxide surface in contact with an electrolyte is ascribed to the H^+ adsorption on/desorption from the surface hydroxyl (OH) groups. The latter form the binding sites for negatively/positively charged adsorbates. The relevant processes are described by the following reversible reactions:

$$\mathrm{M-OH} \leftrightarrow \mathrm{M-O^-} + \mathrm{H_S^+} \tag{1a}$$

$$\mathrm{M-OH_2^+} \leftrightarrow \mathrm{M-OH} + \mathrm{H_S^+} \tag{1b}$$

where, $\mathrm{M\text{-}O^-}$, $\mathrm{M\text{-}OH_2^+}$, $\mathrm{M\text{-}OH}$, and $\mathrm{H_S^+}$ denote deprotonated, protonated, uncharged surface OH group, and surface H^+. In our recent work[25], we have demonstrated an impedance model that incorporates thermodynamic and kinetic properties associated with the H^+ adsorption/desorption processes represented by reactions 1a and 1b. The kinetic rate equations for the two reactions are given as

$$\frac{\mathrm{d[M\text{-}OH]}}{\mathrm{d}t} = c_\mathrm{A}[\mathrm{M\text{-}O^-}]a_\mathrm{S} - r_\mathrm{A}[\mathrm{M\text{-}OH}], \tag{2a}$$

$$\frac{\mathrm{d[M\text{-}OH_2^+]}}{\mathrm{d}t} = c_\mathrm{B}[\mathrm{M\text{-}OH}]a_\mathrm{S} - r_\mathrm{B}[\mathrm{M\text{-}OH_2^+}] \tag{2b}$$

In this model, the kinetic barrier E_c of the binding reactions, which is inevitably modulated by the electrostatic force from adjacent charged sites[28], can vary from site to site. Therefore, the binding site density N_S is assumed to be distributed and to follow a normal distribution in E_c as the following:

$$N_\mathrm{SS}(E) = \frac{N_\mathrm{S}}{\sigma_c\sqrt{2\pi}} \exp\left[-\frac{(E_c - E_{c0})^2}{2\sigma_c^2}\right] \tag{3}$$

where, σ_c is the standard deviation of the distribution, and E_{c0} the energy center for E_c. The H^+ adsorption rate constants c_A and c_B for the reversed reactions (from right to left) in 1a and 1b follow the Arrhenius form:

$$c_{\mathrm{A}}(E) = c_{\mathrm{A}0}\exp\left(-\frac{E_c - E_{c0}}{kT}\right), \quad c_{\mathrm{B}}(E) = c_{\mathrm{B}0}\exp\left(-\frac{E_c - E_{c0}}{kT}\right) \tag{4}$$

where, k is the Boltzmann constant, T the temperature in Kelvin, $c_{\mathrm{A}0}$ and $c_{\mathrm{B}0}$ the values of c_{A} and c_{B} at E_{c0}. In the context of electrochemical impedance spectroscopy (EIS), the binding sties contribute to the impedance by summing up their admittance that is in parallel with the surface in its equivalent circuit. For a set of $N_{\mathrm{SS}}(E)$, $c_{\mathrm{A}}(E)$ and $c_{\mathrm{B}}(E)$, the E_c-distributed site-binding admittance, denoted as $y_{\mathrm{SB}}(E)$, can be solved as:[25]

$$y_{\mathrm{SB}}(E_c) = \frac{sN_{\mathrm{SS}}(E_c)\dfrac{q^2 D_2 K_{\mathrm{B}} a_{\mathrm{S}}}{kTD_1^2}\left\{1 + s\dfrac{1}{D_2}\left[\dfrac{a_{\mathrm{S}}}{c_{\mathrm{A}}(E_c)} + \dfrac{K_{\mathrm{A}}}{c_{\mathrm{B}}(E_c)}\right]\right\}}{1 + \dfrac{s}{D_1}\left[\dfrac{a_{\mathrm{S}} + K_{\mathrm{B}}}{c_{\mathrm{A}}(E_c)} + \dfrac{a_{\mathrm{S}} + K_{\mathrm{A}}}{c_{\mathrm{B}}(E_c)}\right] + \dfrac{s^2}{D_1 c_{\mathrm{A}}(E_c) c_{\mathrm{B}}(E_c)}} \tag{5}$$

where, K_{A} and K_{B} are the equilibrium constants for 1a and 1b, respectively, a_{S} the $\mathrm{H_S^+}$ activity, $s = j\omega$ with j as the imaginary unit and ω angular frequency, $D_1 = K_{\mathrm{A}}K_{\mathrm{B}} + K_{\mathrm{B}}a_{\mathrm{S}} + a_{\mathrm{S}}^2$, and $D_2 = K_{\mathrm{A}}K_{\mathrm{B}} + 4K_{\mathrm{A}}a_{\mathrm{S}} + a_{\mathrm{S}}^2$. The site-binding impedance z_{SB}, i.e. the reciprocal of y_{SB} in eq 5, can be decomposed to a sum of first-order partial fractions[25]:

$$z_{\mathrm{SB}} = \frac{1}{y_{\mathrm{SB}}} = \frac{1}{sC_{\mathrm{buff}}} + \frac{R_{\mathrm{p}}}{1 + s\tau_{\mathrm{p}}} + R_{\mathrm{s}} \tag{6}$$

where, C_{buff} is the buffer capacitance, R_{p} and R_{s} the effective resistive component respectively associated with reaction 1a and 1b, and τ_{p} the time constant associated with the reactions. The expressions of these intermediate parameters are detailed in Supporting Information (SI). Eq 6 can be described using the marked equivalent circuit depicted in Figure 1a. The total site-binding admittance Y_{SB} for all the sites should be the integral of $y_{\mathrm{SB}}(E_c)$ over the whole energy range, i.e. $Y_{\mathrm{SB}} = \int y_{\mathrm{SB}}(E_c)\mathrm{d}E_c$ as represented in its discrete form in the figure.

The capacitance of the electrical double layer (EDL) C_{DL}, also illustrated in Figure 1a, is in parallel with the Y_{SB} network[29]. Therefore, the total electrochemical impedance for the oxide/liquid interface, denoted by Z_{int}, can be expressed as:

$$Z_{int} = \frac{1}{sC_{DL} + Y_{SB}} \tag{7}$$

Because the potentiometric LFN correlates excellently to the real part of its electrochemical impedance spectrum[16], the real part of the impedance can, thus, represent the LFN originating from the oxide/electrolyte interface. It is calculated by,

$$S_V^n = 4kT\mathrm{Re}(Z_{int}) \tag{8}$$

where, S_V^n denote the voltage noise power spectrum.

Experimental

For electrode fabrication, a 100-nm thick Ti layer was first sputter-deposited on a glass wafer. This was followed by the sputter-deposition of a 40-nm thick TiN layer. For sensing surface, ultrathin ALD TiO_2 layers of three different thicknesses were prepared at 200 °C with $TiCl_4$ and H_2O as the reaction precursors for 20, 40, and 60 cycles. Transmission electron microscopy (TEM) was used to inspect the detailed structure of the layered stacks. On each sample, a circular liquid reservoir of 10 mm diameter was defined using epoxy.

To evaluate the TiO_2 as a sensing surface, the *p*H sensitivity, S_{pH}, defined as the variation of surface electrical potential, φ_S, per unit *p*H change, was measured using a Bio-Logic VSP-300 potentiostat via a three-electrode setup, as depicted in Figure 1b. An Ag/AgCl/3 M NaCl reference electrode (RE) and a Pt wire electrode as the counter electrode were submerged in the buffer solution (Merck Titrisol) with *p*H value ranging from 4 to 10. The measured S_{pH} for the three samples are listed in Table 1. The EIS measurement was performed with the same

measurement setup. The impedance spectrum was measured at 10 mV root-mean-square (RMS) AC from 100 mHz to 1 MHz. The measurement data was averaged over 30 cycles for each frequency point. The sampling *p*H was 5, 7, and 9 for the EIS measurement.

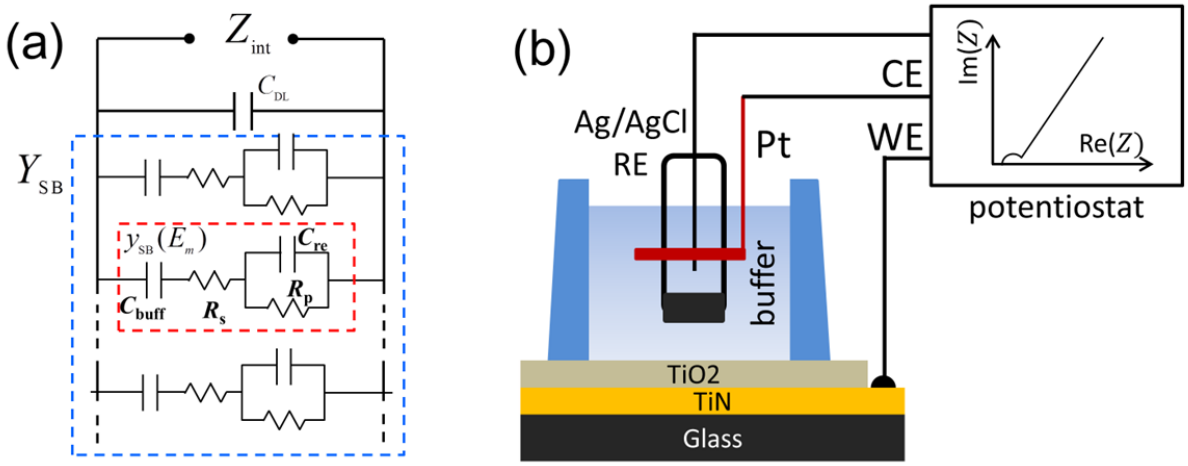

Figure 1. (a) Equivalent circuit of the oxide/electrolyte interfacial impedance, with the distributed Y_{SB} in its discrete representation. (b) Schematics of the electrode cell and the EIS measurement setup.

TABLE 1. Parameters for modeling the noise of the three processed samples.

parameter	20 cycle			40 cycle			60 cycle		
	*p*H5	*p*H7	*p*H9	*p*H5	*p*H7	*p*H9	*p*H5	*p*H7	*p*H9
[1]N_S, 10^{18} m^{-2}	10.1	10.0	9.9	9.0	9.0	8.7	6.9	7.0	5.7
[1]C_{DL}, Fm^{-2}	0.26	0.26	0.27	0.26	0.26	0.27	0.26	0.26	0.24
[2]c_{A0}, M^{-1}s^{-2}	1.9×10^{-2}	7.8×10^{-3}	4.8×10^{-1}	8.2×10^{-1}	78.8	2.0×10^{2}	2.2×10^{4}	7.5×10^{3}	1.7×10^{4}
[2]c_{B0}, M^{-1}s^{-2}	5.9×10^{-26}	1.3×10^{-14}	6.4×10^{-19}	2.6×10^{-2}	2.4×10^{-4}	8.7×10^{-6}	2.2×10^{1}	1.6×10^{2}	2.9×10^{2}
[2]σ_c, eV	0.337	0.327	0.318	0.231	0.179	0.182	0.121	0.116	0.114
[3]pK$_A$, -log$_{10}$(K_A)		7.7			7.7			7.7	
[3]pK$_B$, -log$_{10}$(K_B)		4.7			4.7			4.7	
[4]S_{pH}, mV/*p*H		55.4			55			53.9	

[1]Calculated via S_{pH} (see SI). [2]Fitting. [3]Reported[30,31]. [4]Measured

Model analysis

A. Evaluation of the modeling parameters

With the aid of the S_{pH} measurement, the values of a_S, C_{DL} and N_S were obtained by solving by the relevant equations in the classic site-binding model [26], which is detailed in SI. As seen in our recent work[25], K_A and K_B of TiO_2 tend to be invariable. They can be assigned with well-established reported values, as listed in Table 1 in their logarithm form, i.e. $pK_A = -\log(K_A)$ and $pK_B = -\log(K_B)$. With a_S, N_S and C_{DL} as modeling input, the kinetic parameters c_{A0} and c_{B0} as well as σ_c in eqs 3 and 4 were determined by numerically fitting the real part of eq 5, i.e. Re(Z_{int}), to that of the measured impedance. The real part of the measured impedance also includes the electrolyte series resistance, and it was subtracted from the measured data in our fitting procedure. As the capacitance of the TiO_2 layer that is in series with the interfacial components is assumed to be pure capacitive, it does not contribute to the real part of the impedance. The measured S_V^n (from the real part of the impedance) for all the samples is excellently fitted by the theoretical S_V^n, calculated via eq 6, in the frequency interval 0.1-10 Hz. The values of the modeling parameters are also given in Table. 1. In what follows for noise analysis, we will focus on *p*H=7, with an excellent fitting detailed in Figure 2.

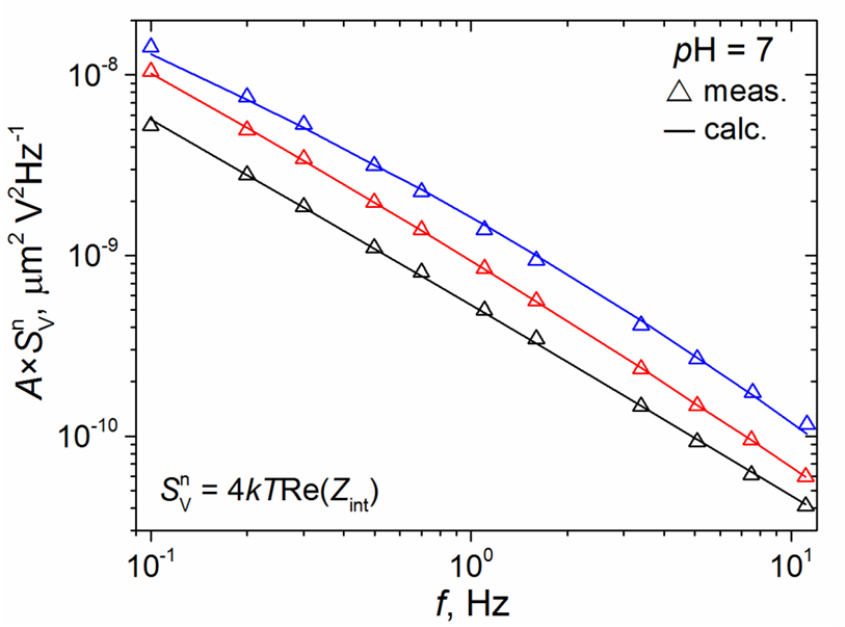

Figure 2. Comparison between simulated noise spectrum density (depicted as solid lines) and the experimental data calculated from the real part of the measured impedance (depicted as triangels). Black, red and blue represent 20, 40 and 60 cycle samples, respectively.

B. Noise dependence on the site-binding admittance Y_{SB}

The interfacial LFN, in terms of the interfacial impedance, comprises concurrent contributions from C_{DL} and Y_{SB}, as indicated in eq 7; C_{DL}, as a pure capacitive component at these frequencies[32], is not related to the dynamic nature of the binding reactions, while Y_{SB} directly results from these dynamic processes. It is, thus, only Y_{SB} that can reflect the correlation of the surface dynamics to the noise. For noise study, investigation of the real component of Y_{SB} is relevant because the interfacial noise, as expressed by eq 6, is linked to $\mathrm{Re}(Y_{SB})$ via the following expression:

$$\mathrm{Re}(Z_{int}) = \frac{1}{|Y_{int}|^2}\mathrm{Re}(Y_{int}) = \frac{1}{|Y_{int}|^2}\mathrm{Re}(Y_{SB}) \tag{9}$$

where, the second equation is based on $\mathrm{Re}(Y_{\mathrm{int}})=\mathrm{Re}(Y_{\mathrm{SB}})$, as illustrated in the equivalent circuit in Figure 1a. Specifically, the sample-dependent trend of $\mathrm{Re}(Y_{\mathrm{SB}})$ extracted from the measurement, as depicted in Figure 3a, becomes the benchmark to which the trend of $\mathrm{Re}(Y_{\mathrm{SB}})$ calculated with the sample-dependent dynamic properties will be compared, as will be discussed momentarily.

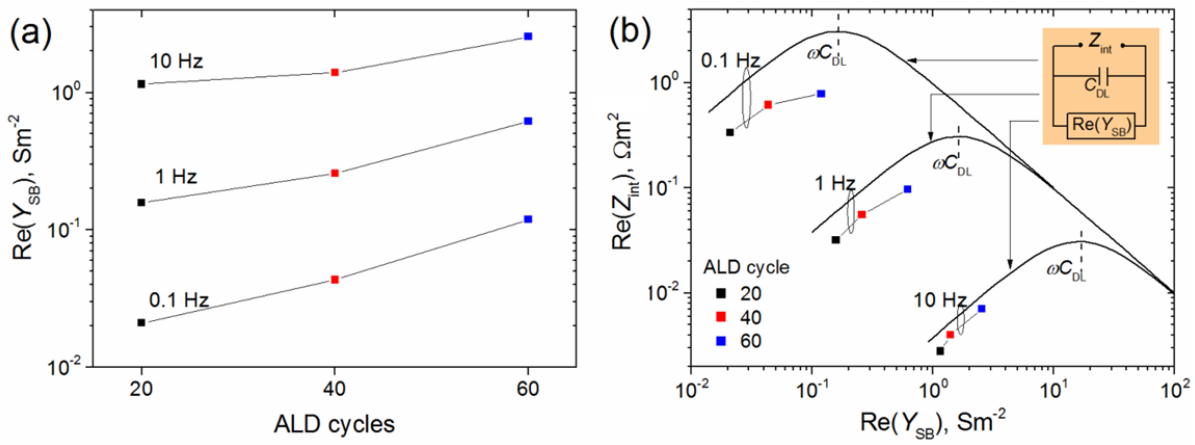

Figure 3. (a) $\mathrm{Re}(Y_{\mathrm{SB}})$ extracted from the EIS measurement at three different frequencies for the samples. (b) Dependence of $\mathrm{Re}(Z_{\mathrm{int}})$ on $\mathrm{Re}(Y_{\mathrm{SB}})$ extracted from the EIS measurement at the same frequencies for all the samples. The dependence of $\mathrm{Re}(Z_{\mathrm{int}})$ on $\mathrm{Re}(Y_{\mathrm{SB}})$ by omitting $\mathrm{Im}(Y_{\mathrm{SB}})$ is also depicted as solid curves.

The dependence of $\mathrm{Re}(Z_{\mathrm{int}})$ on $\mathrm{Re}(Y_{\mathrm{SB}})$ extracted from the EIS measurement, as represented with the colored squares in Figure 3b, can be analyzed semi-quantitatively by removing $\mathrm{Im}(Y_{\mathrm{SB}})$ from the Z_{int} network (see the inset for the equivalent circuit). As the solid curves show in Figure 3b for all three frequencies, $\mathrm{Re}(Z_{\mathrm{int}})$ linearly increases with $\mathrm{Re}(Y_{\mathrm{SB}})$ when $\mathrm{Re}(Y_{\mathrm{SB}})$ is below the susceptance of C_{DL} at a specified frequency, i.e. ωC_{DL}. This predicted trend is followed well by the observed $\mathrm{Re}(Z_{\mathrm{int}})-\mathrm{Re}(Y_{\mathrm{SB}})$ relation, as shown in the figure. However, the trend

reverses from linearly increasing to decreasing in the log-log scale once $\mathrm{Re}(Y_{\mathrm{SB}})$ goes beyond ωC_{DL}. Therefore, the dependence of LFN on $\mathrm{Re}(Y_{\mathrm{SB}})$ is primarily determined by the relative size of ωC_{DL} to $\mathrm{Re}(Y_{\mathrm{SB}})$ at a given frequency.

C. Average of the distributed properties

As discussed in section 2, N_{S}, c_{A} and c_{B} are all dependent on E_c. At a given frequency, as discussed in our recent work[25], only a fraction of the sites having an appropriate c_{A} and c_{B} can contribute to Z_{int}, and thus the noise. It is practical to define representative values for such E_c-distributed properties for the whole surface in order to facilitate the analysis of the noise behavior. This can be achieved by calculating the weighted average $\langle E_{c0} - E_c \rangle = \dfrac{\int (E_{c0} - E_c)\,\mathrm{Re}\left[y_{\mathrm{SB}}(E_c)\right]\mathrm{d}E_c}{\int \mathrm{Re}\left[y_{\mathrm{SB}}(E_c)\right]\mathrm{d}E_c}$ with $\mathrm{Re}\left[y_{\mathrm{SB}}(E_c)\right]$ as the weighting factor owing to its physical role in determining the noise properties. In Figure 4, the dependence of $\mathrm{Re}\left[y_{\mathrm{SB}}(E_c)\right]$ on E_c is depicted at (a) 1 Hz and (b) 10 Hz. Only the sites with $N_{\mathrm{SS}}(E_c)$, and thus the corresponding $c_{\mathrm{A}}(E_c)$ and $c_{\mathrm{B}}(E_c)$, within narrow ranges around the peaks of $y_{\mathrm{SB}}(E)$ contribute effectively. For simplicity, their average $N_{\mathrm{SS}}(E_c)$, $c_{\mathrm{A}}(E_c)$ and $c_{\mathrm{B}}(E_c)$, i.e. $\langle N_{\mathrm{SS}} \rangle$, $\langle c_{\mathrm{A}} \rangle$ and $\langle c_{\mathrm{B}} \rangle$, are defined by the following:

$$\langle c_{\mathrm{A}} \rangle = c_{\mathrm{A0}} \exp\frac{\langle E_{c0} - E_c \rangle}{kT}, \quad \langle c_{\mathrm{B}} \rangle = c_{\mathrm{B0}} \exp\frac{\langle E_{c0} - E_c \rangle}{kT} \tag{10a}$$

$$\langle N_{\mathrm{SS}} \rangle = \frac{N_{\mathrm{S}}}{\sigma_{\mathrm{E}}\sqrt{2\pi}} \exp - \frac{\langle E_{c0} - E_c \rangle^2}{2\sigma_{\mathrm{E}}^2} \tag{10b}$$

The averaged $y_{\mathrm{SB}}(E_c)$, $\langle y_{\mathrm{SB}} \rangle$, can then be represented as well by substituting $N_{\mathrm{SS}}(E_c)$, $c_{\mathrm{A}}(E_c)$ and $c_{\mathrm{B}}(E_c)$ in eq 5 with their average values calculated with eqs 10a and 10b.

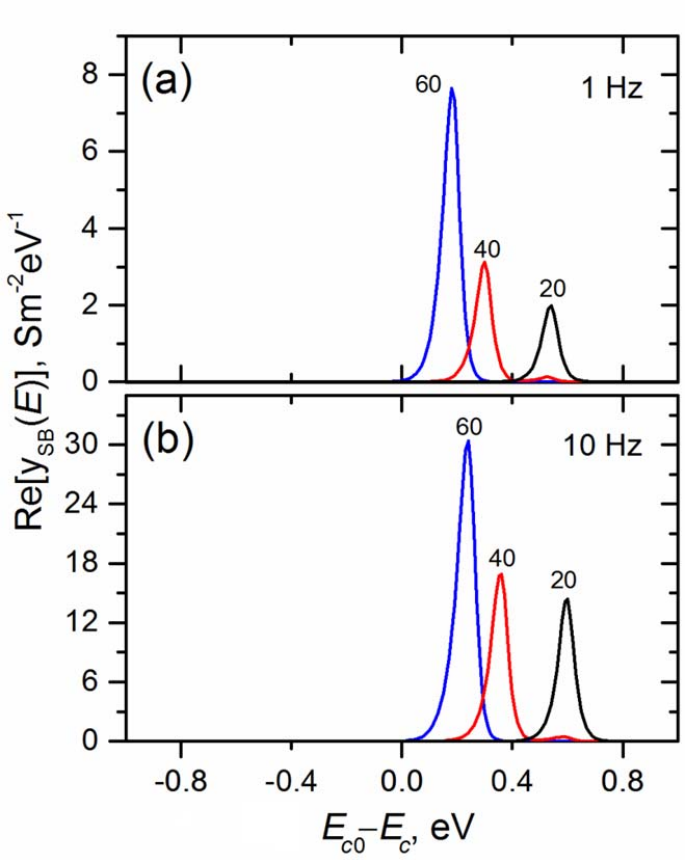

Figure 4. Re(y_{SB}) dependent on the reaction energy barreir E_c at (a) 1 Hz and (b) 10 Hz for the samples.

Results and discussion

In Figure 5a, $\langle c_A \rangle$ and $\langle c_B \rangle$ are depicted in order of ALD cycles at three different frequencies, 0.1, 1, and 10 Hz. As seen, both $\langle c_A \rangle$ and $\langle c_B \rangle$ are dependent on f; at a given f, $\langle c_A \rangle$ is almost identical for all samples independent of the number of deposition cycles, but $\langle c_B \rangle$ increases by 10 orders of magnitude as the ALD process increases from 20 to 60 cycles. To elucidate this, the schematic frequency response of the real part of a single branch y_{SB} is plotted in Figure 5b, where Re(Y_{SB}), as the envelope of several y_{SB} branches, is also plotted. It is seen that each

branch contributes to $\mathrm{Re}(Y_{SB})$ mainly near its corner frequency f_c, which corresponds to the admittance contribution within a narrow E_c range at a certain frequency, as shown in Figure 4. Therefore, at a given measurement frequency f_M, only the branches that have f_c close to f_M will contribute to $\mathrm{Re}(Y_{SB})$. The relationship between f_c and the surface properties was found to be $f_c \approx \frac{a_S c_A(E_c)}{2\pi}$ for any branch (see SI). At a specified f_M, $\langle c_A \rangle$ can be estimated with:

$$\langle c_A \rangle = \frac{2\pi}{a_S} f_M \tag{11}$$

Since a_S is kept constant by a large C_{buff} for similar surfaces at the same pH, $\langle c_A \rangle$ estimated via eq 11 will be determined mainly by f_M and is not expected to vary much from sample to sample. Eq 11 also clearly indicates that at low f_M, the sites with low $\langle c_A \rangle$ (high kinetic barrier E_c) contribute dominantly to $\mathrm{Re}(Y_{SB})$ and thus LFN, while those with high $\langle c_A \rangle$ (low E_c) contribute only at higher f_M. However, since Y_{SB} is in parallel with C_{DL}, the contribution from the sites with low E_c to the noise will be shorted by C_{DL} at high frequencies. Since f_c is observed to be independent of c_B, it becomes apparent that the $-O^-$ sites, rather than the neutral –OH sites, determine the surface dynamics and thus the noise, as a result of the much larger reaction rate of the $-O^-$ sites than that of the –OH sites. At a given f_M, the –OH sites behave as if they "freeze out" compared to the $-O^-$ sites. By substituting $\langle c_A \rangle$ and $\langle c_B \rangle$ for each samples in eq 5, $\mathrm{Re}[\langle y_{SB} \rangle]$, normalized with $\frac{q^2 N_{SS}(E)}{kT}$, is depicted in Figure 5c at the three frequencies. As seen, the increment of the normalized $\mathrm{Re}[\langle y_{SB} \rangle]$ at a given frequency is less than a factor of 2 from 20 to 60 growth cycles, which is the direct result of the invariability of $\langle c_A \rangle$ and thus distinctly differs from the observed trend of $\mathrm{Re}(Y_{SB})$ in Figure 3a.

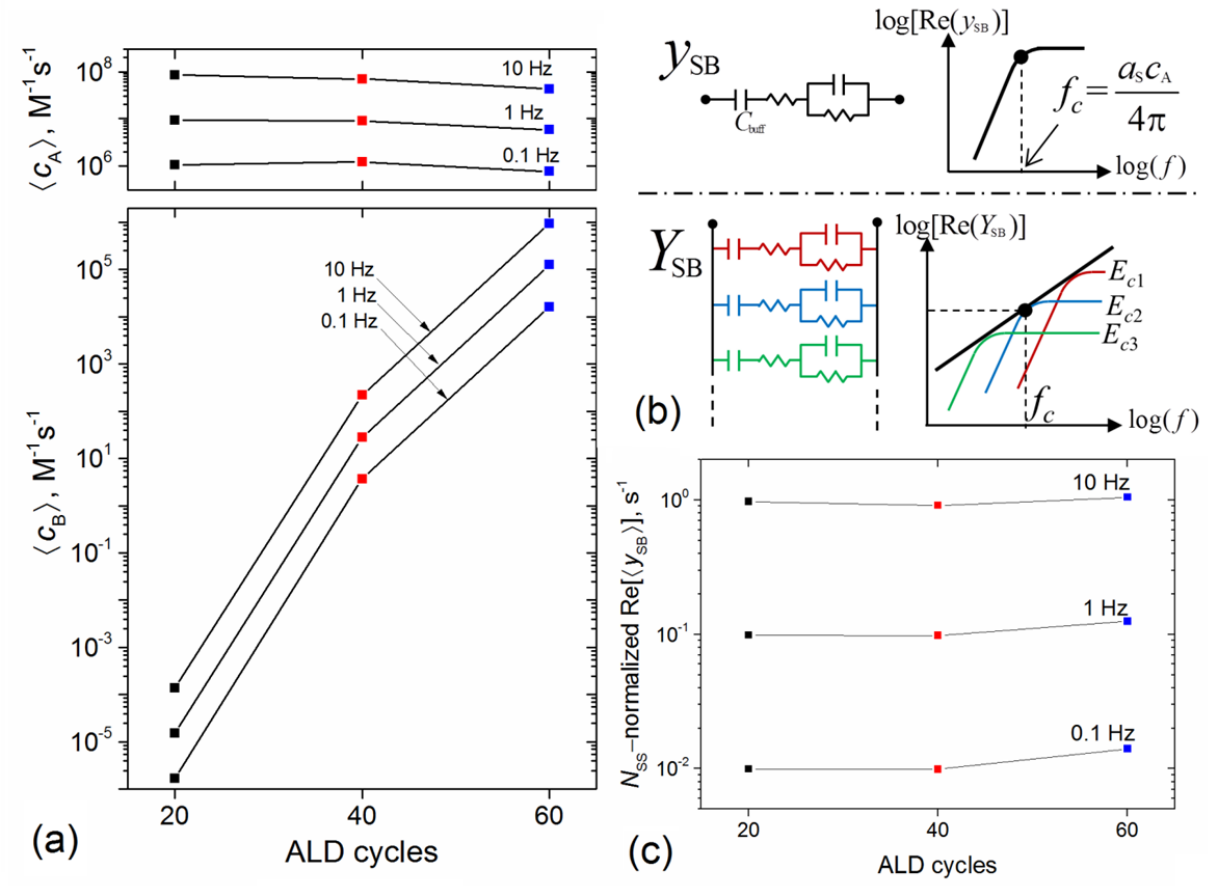

Figure 5. (a) Sample-dependent $\langle c_A \rangle$ and $\langle c_B \rangle$ at three different frequencies. (b) Schematic frequency responses of $\mathrm{Re}(y_{SB})$ and $\mathrm{Re}(Y_{SB})$. (c) N_{SS}-normalized $\mathrm{Re}[\langle y_{SB} \rangle]$ in order of the samples at the three different frequencies.

To investigate the influence of $\langle N_{SS} \rangle$ on LFN, $\langle N_{SS} \rangle$ was first calculated via eq 10b and depicted for the three samples in Figure 6a at the three frequencies. $\langle N_{SS} \rangle$ is found to increase with the cycle number from 20 to 60 cycles at a given f. This behavior agrees with the observed sample-dependent trend of $\mathrm{Re}(Y_{SB})$ in Figure 3a. Using $\langle N_{SS} \rangle$, $\langle c_A \rangle$, and $\langle c_B \rangle$ for each sample, $\mathrm{Re}(\langle y_{SB} \rangle)$ was then calculated and depicted in Figure 6b, again for the three frequencies. $\mathrm{Re}(\langle y_{SB} \rangle)$ in Figure 6b resembles well $\mathrm{Re}(Y_{SB})$ in Figure 3a. It is therefore apparent that $\langle N_{SS} \rangle$,

not $\langle c_A \rangle$ and $\langle c_B \rangle$, plays the dominant role in determining the amplitude of the LFN. One can notice that the ALD cycle dependence of the total N_S, as seen in Table 1, is opposite to that of $\langle N_{SS} \rangle$. It should be noted that $\langle N_{SS} \rangle$ represents the responding fraction of the binding sites, and it is not directly correlated to the total N_S. It is observed by our TEM analysis[25] that the TiN film is characterized by fine columnar TiN crystals. The columnar growth can result in a significant increase in effective area with dense nanoscale features, and thus N_S. This TiN surface becomes replaced by an ALD TiO_2 surface with a reduced density of such features as well as a reduced surface roughness, which can explain the decreasing trend in N_S with increasing the number of ALD cycles (Table 1).

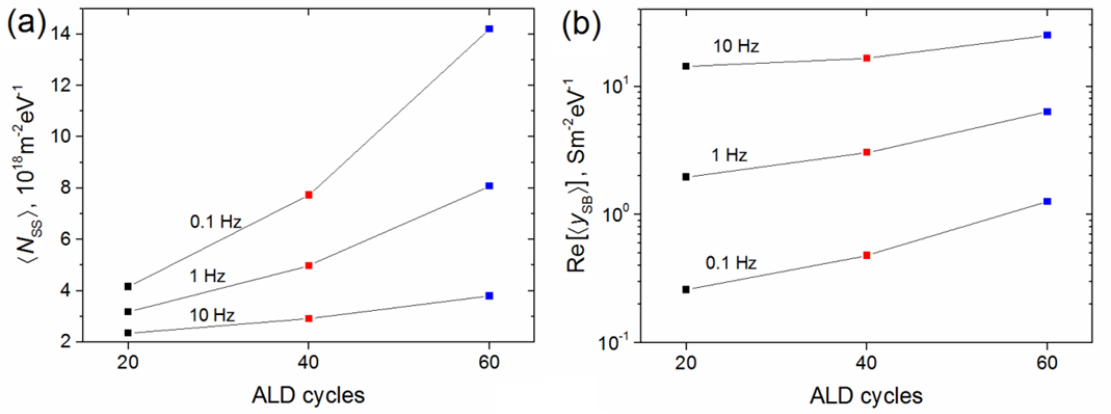

Figure 6. (a) $\langle N_{SS} \rangle$ and (b) $\mathrm{Re}\left[\langle y_{SB} \rangle\right]$ in the order of the samples at three different frequencies.

As shown in Figure 7 with three site-binding branches characterized by E_{c1} to E_{c3} for illustration, the noise spectrum envelope consists of contributions from distributed site-binding branches with different kinetic barriers E_c. It is the sites with large E_c that would contribute most to the noise in the low-frequency regime; the amplitude of the LFN is primarily determined by

the N_{ss} with large E_c. Therefore, to minimize the LFN, reducing the N_{ss} with large E_c can be an effective approach.

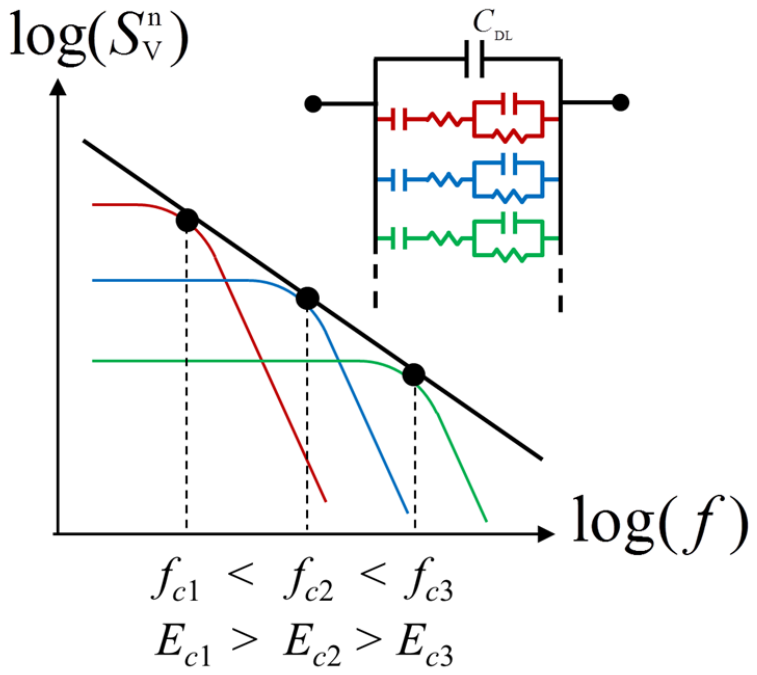

Figure 7. Schematic low-frequency noise spectrum. The three colored lines illustrate contributions from three site-binding reaction branches with different kinetic energy barriers, E_{c1}, E_{c2}, and E_{c3}.

CONCLUSIONS

Electrochemical impedance modeling has been used to correlate the oxide/electrolyte interfacial LFN to the dynamic properties of H^+ binding/de-binding reactions with the surface OH group as the binding sites. The dependence of the real part of the site-binding admittance $\mathrm{Re}(Y_{SB})$ on the reaction rate constants and the binding site density per unit kinetic barrier is investigated to account for the observed trend of LFN, yielding conclusions as follows:

1. This dependence of the interfacial LFN, $4kT\,\mathrm{Re}(Z_{\mathrm{int}})$, on $\mathrm{Re}(Y_{\mathrm{SB}})$ is generally determined by the relative size of the susceptance of C_{DL} to $\mathrm{Re}(Y_{\mathrm{SB}})$, at a given frequency. When $\mathrm{Re}(Y_{\mathrm{SB}})$ is considerably smaller than ωC_{DL}, the LFN linearly increases with $\mathrm{Re}(Y_{\mathrm{SB}})$; as $\mathrm{Re}(Y_{\mathrm{SB}})$ is closer to and eventually larger than ωC_{DL}, the dependence of the noise on $\mathrm{Re}(Y_{\mathrm{SB}})$ transits, gradually, from linearly increasing to linearly decreasing on a log scale.

2. The binding sites with large kinetic barriers dominate the noise in the low frequency regime. And it is $\langle N_{\mathrm{SS}} \rangle$, rather than N_{S}, that decisively determines the amplitude of the LFN. Thus, reducing the number of such sites can be an effective way to minimize the LFN.

ASSOCIATED CONTENT

Supporting Information (will be available online).

1. Evaluation of static properties a_{S}, C_{Stern}, and N_{S}

2. Simplified expression of τ_{p}, R_{s}, and R_{p}

3. Dependence of f_{c} on surface properties

AUTHOR INFORMATION

Corresponding Author

*E-mail: solomonp@us.ibm.com

*E-mail: zhen.zhang@angstrom.uu.se.

ACKNOWLEDGMENT

Fruitful discussions with Chengyu Wen are gratefully acknowledged. This work was supported by the Swedish Research Council (VR 2014-5588), Göran Gustafssons Foundation (GG 1459B), Carl Tryggers Foundation (CTS14-527), Stiftelsen Olle Engkvist Byggmästare (2016/39), the Wallenberg Academy Fellow Program, and the Swedish Strategic Research Foundation (5th Ingvar Carlsson Award and 6th Future Research Leader programs).

REFERENCES

(1) Duan, X.; Li, Y.; Rajan, N. K.; Routenberg, D. A.; Modis, Y.; Reed, M. A. Quantification of the Affinities and Kinetics of Protein Interactions Using Silicon Nanowire Biosensors. *Nat Nano* **2012**, *7* (6), 401–407.

(2) Bedner, K.; Guzenko, V. A.; Tarasov, A.; Wipf, M.; Stoop, R. L.; Rigante, S.; Brunner, J.; Fu, W.; David, C.; Calame, M.; Gobrecht, J.; Schönenberger, C. Investigation of the Dominant 1/f Noise Source in Silicon Nanowire Sensors. *Sensors Actuators, B Chem.* **2014**, *191*, 270–275.

(3) Heller, I.; Chatoor, S.; M??nnik, J.; Zevenbergen, M. A. G.; Oostinga, J. B.; Morpurgo, A. F.; Dekker, C.; Lemay, S. G. Charge Noise in Graphene Transistors. *Nano Lett.* **2010**, *10* (5), 1563–1567.

(4) Stoop, R. L.; Thodkar, K.; Molecular, I. D. C.; Valencia, U. De; Schönenberger, C.; Calame, M. Charge Noise in Organic Electrochemical Transistors. *Phys. Rev. Appl.* **2017**, *14009*, 1–8.

(5) Bergveld, P. Thirty Years of ISFETOLOGY: What Happened in the Past 30 Years and What May Happen in the next 30 Years. *Sensors Actuators, B Chem.* **2003**, *88* (1), 1–20.

(6) Rothberg, J. M.; Hinz, W.; Rearick, T. M.; Schultz, J.; Mileski, W.; Davey, M.; Leamon,

J. H.; Johnson, K.; Milgrew, M. J.; Edwards, M.; Hoon, J.; Simons, J. F.; Marran, D.; Myers, J. W.; Davidson, J. F.; Branting, A.; Nobile, J. R.; Puc, B. P.; Light, D.; Clark, T. a; Huber, M.; Branciforte, J. T.; Stoner, I. B.; Cawley, S. E.; Lyons, M.; Fu, Y.; Homer, N.; Sedova, M.; Miao, X.; Reed, B.; Sabina, J.; Feierstein, E.; Schorn, M.; Alanjary, M.; Dimalanta, E.; Dressman, D.; Kasinskas, R.; Sokolsky, T.; Fidanza, J. a; Namsaraev, E.; McKernan, K. J.; Williams, A.; Roth, G. T.; Bustillo, J. An Integrated Semiconductor Device Enabling Non-Optical Genome Sequencing. *Nature* **2011**, *475* (7356), 348–352.

(7) Toumazou, C.; Shepherd, L. M.; Reed, S. C.; Chen, G. I.; Patel, A.; Garner, D. M.; Wang, C.-J. a; Ou, C.-P.; Amin-Desai, K.; Athanasiou, P.; Bai, H.; Brizido, I. M. Q.; Caldwell, B.; Coomber-Alford, D.; Georgiou, P.; Jordan, K. S.; Joyce, J. C.; La Mura, M.; Morley, D.; Sathyavruthan, S.; Temelso, S.; Thomas, R. E.; Zhang, L. Simultaneous DNA Amplification and Detection Using a pH-Sensing Semiconductor System. *Nat. Methods* **2013**, *10* (7), 641–646.

(8) Jakobson, C. G.; Nemirovsky, Y. I/f Noise in Ion Sensitive Field Effect Transistors from Subthreshold to Saturation. *IEEE Trans. Electron Devices* **1999**, *46* (1), 259–261.

(9) Hassibi, A.; Navid, R.; Dutton, R. W.; Lee, T. H. Comprehensive Study of Noise Processes in Electrode Electrolyte Interfaces. *J. Appl. Phys.* **2004**, *96* (2), 1074–1082.

(10) Deen, M. J.; Shinwari, M. W.; Ranuárez, J. C.; Landheer, D. Noise Considerations in Field-Effect Biosensors. *J. Appl. Phys.* **2006**, *100* (7), 74703–74708.

(11) Rajan, N. K.; Routenberg, D. A.; Chen, J.; Reed, M. A. 1/f Noise of Silicon Nanowire BioFETs. *IEEE Electron Device Lett.* **2010**, *31* (6), 615–617.

(12) Rajan, N. K.; Routenberg, D. A.; Reed, M. A. Optimal Signal-to-Noise Ratio for Silicon Nanowire Biochemical Sensors. *Appl. Phys. Lett.* **2011**, *98* (26), 2–4.

(13) Tarasov, A.; Fu, W.; Knopfmacher, O.; Brunner, J.; Calame, M.; Schönenberger, C. Signal-to-Noise Ratio in Dual-Gated Silicon Nanoribbon Field-Effect Sensors. *Appl. Phys. Lett.* **2011**, *98* (1), 2011–2014.

(14) Go, J.; Nair, P. R.; Alam, M. A. Theory of Signal and Noise in Double-Gated Nanoscale Electronic pH Sensors. *J. Appl. Phys.* **2012**, *112* (3), 34516.

(15) Zhang, D.; Gao, X.; Chen, S.; Norström, H.; Smith, U.; Solomon, P.; Zhang, S. L.; Zhang, Z. An Ion-Gated Bipolar Amplifier for Ion Sensing with Enhanced Signal and Improved Noise Performance. *Appl. Phys. Lett.* **2014**, *105* (8), 82102.

(16) Zhang, D.; Must, I.; Netzer, N. L.; Xu, X.; Solomon, P.; Zhang, S. L.; Zhang, Z. Direct Assessment of Solid-Liquid Interface Noise in Ion Sensing Using a Differential Method. *Appl. Phys. Lett.* **2016**, *108* (15), 151603.

(17) Zhuge, J.; Wang, R.; Huang, R.; Tian, Y.; Zhang, L.; Kim, D. W.; Park, D.; Wang, Y. Investigation of Low-Frequency Noise in Silicon Nanowire MOSFETs. *IEEE Electron Device Letters*. 2009, pp 57–60.

(18) Haemmerli, A.; Janata, J.; Brophy, J. J. Equilibrium Noise in Ion Selective Field Effect Transistors. *J. Electrochem. Soc.* **1982**, *129* (10), 2306–2312.

(19) Barabash, P. R.; Cobbold, R. S. C. Basic Limitations of Isfet and Silicon Pressure Transducers: Noise Theory, Models and Device Scaling. *Sensors and Actuators* **1983**, *4* (C), 427–438.

(20) Hauf, M. V.; Hess, L. H.; Howgate, J.; Dankerl, M.; Stutzmann, M.; Garrido, J. A. Low-Frequency Noise in Diamond Solution-Gated Field Effect Transistors. *Appl. Phys. Lett.* **2010**, *97* (9), 093504.

(21) Clément, N.; Nishiguchi, K.; Dufreche, J. F.; Guerin, D.; Fujiwara, A.; Vuillaume, D. A

Silicon Nanowire Ion-Sensitive Field-Effect Transistor with Elementary Charge Sensitivity. *Appl. Phys. Lett.* **2011**, *98* (1), 1–4.

(22) Chen, S.; Van Den Berg, A.; Carlen, E. T. Sensitivity and Detection Limit Analysis of Silicon Nanowire Bio(chemical) Sensors. *Sensors Actuators, B Chem.* **2015**, *209*, 486–489.

(23) Georgakopoulou, K.; Birbas, A.; Spathis, C. Modeling of Fluctuation Processes on the Biochemically Sensorial Surface of Silicon Nanowire Field-Effect Transistors. *J. Appl. Phys.* **2015**, *117* (10), 104505.

(24) Crosser, M. S.; Brown, M. A.; McEuen, P. L.; Minot, E. D. Determination of the Thermal Noise Limit of Graphene Biotransistors. *Nano Lett.* **2015**, *15* (8), 5404–5407.

(25) Zhang, D.; Solomon, P.; Zhang, S. L.; Zhang, Z. Low-Frequency Noise Originating from the Dynamic Hydrogen Ion Reactivity at the Solid/liquid Interface of Ion Sensors. *Sensors and Actuators B: Chem. to be published*

(26) van Hal, R. E. G.; Eijkel, J. C. T.; Bergveld, P. A General Model to Describe the Electrostatic Potential at Electrolyte Oxide Interfaces. *Adv. Colloid Interface Sci.* **1996**, *69* (1–3), 31–62.

(27) Yates, D. E.; Levine, S.; Healy, T. W. Site-Binding Model of the Electrical Double Layer at the Oxide/water Interface. *J. Chem. Soc. Faraday Trans. 1 Phys. Chem. Condens. Phases* **1974**, *70* (0), 1807.

(28) Potapenko, D. V.; Gomes, G. T.; Osgood, R. M. Correlation of H Adsorption Energy and Nanoscale Elastic Surface Strain on Rutile TiO2(110). *J. Phys. Chem. C* **2016**, *120* (38), 21373–21380.

(29) Brug, G. J.; van den Eeden, A. L. G.; Sluyters-Rehbach, M.; Sluyters, J. H. The Analysis

of Electrode Impedances Complicated by the Presence of a Constant Phase Element. *J. Electroanal. Chem.* **1984**, *176* (1–2), 275–295.

(30) Schindler, P. W.; Gamsjäger, H. Acid - Base Reactions of the TiO2 (Anatase) - Water Interface and the Point of Zero Charge of TiO2 Suspensions. *Kolloid-Zeitschrift Zeitschrift für Polym.* **1972**, *250* (7), 759–763.

(31) Ashida, M.; Sasaki, M.; Kan, H.; Yasunaga, T.; Hachiya, K.; Inoue, T. Kinetics of Proton Adsorption-Desorption at TiO2-H2O Interface by Means of Pressure-Jump Technique. *J. Colloid Interface Sci.* **1978**, *67* (2), 219–225.

(32) Bousse, L.; Bergveld, P. On the Impedance of the Silicon Dioxide/electrolyte Interface. *J. Electroanal. Chem. Interfacial Electrochem.* **1983**, *152* (1–2), 25–39.

For TOC only